Cooperative phosphorus and chromium doping induced electronic and morphological dual modulation in NiMoO$_4$ hydrate for energy-efficient urea-assisted hydrogen production

Yanyan Li [a], Haoran Guo [a], Yao Zhang [a,b], Rui Song [a,*]

[a] *School of Chemical Sciences, University of Chinese Academy of Sciences, 19 Yuquan Road, Shijingshan District, Beijing 100049, PR China*
[b] *School of Materials and Chemical Engineering, Xuzhou University of Technology, Xuzhou 221018, PR China*

ARTICLE INFO

ABSTRACT

The electrochemical oxidation of urea presents a promising avenue for hydrogen production with reduced energy consumption. Therefore, developing an efficient bifunctional electrocatalyst capable of catalyzing both the urea oxidation reaction (UOR) and hydrogen evolution reaction (HER) is of prominent importance. Herein, a cooperative P and Cr co-doped NiMoO$_4$ hydrate electrode (P/Cr$_{60}$-NiMoO$_4$) is developed as a self-supported bifunctional electrode for energy-efficient urea-assisted H$_2$ production. Benefiting from the cooperativity of both dopants, the P/Cr$_{60}$-NiMoO$_4$ electrocatalyst exhibits remarkable performance in UOR and HER, achieving 1.33 V and 35.7 mV at 10 mA cm^{-2}, respectively. Moreover, the utilization of P/Cr$_{60}$-NiMoO$_4$ as a dual-functional catalyst only needs 1.35 V to reach 10 mA cm^{-2} in 1 M KOH electrolyte with 0.33 M urea, representing a reduction of 180 mV compared to conventional water electrocatalysis devices (OER//HER systems). Theoretical calculations based on density functional theory reveal that the superior activity of the P/Cr-incorporation system can be attributed to its ability to enhance interface electron concentration, promote electron transfer, and reduce the free energy barriers associated with both UOR and HER.

1. Introduction

Urea-assisted water electrolysis is a technology that utilizes the anodic urea oxidation reaction (UOR) and cathodic hydrogen evolution reaction (HER) to simultaneously produce hydrogen and purify urea-rich wastewater. [1–3] Compared to conventional water splitting, UOR has a more favorable thermodynamic potential with a significantly lower cell potential of 0.37 V. [4,5] Nevertheless, the challenge lies in the complexity of UOR (i.e., CO(NH$_2$)$_2$ + 6OH$^-$ → N$_2$ + CO$_2$ + 5 H$_2$O + 6e$^-$, UOR), which exhibits sluggish kinetics due to a six-electron transfer process and necessitates highly active catalysts to promote reaction rates. [6–8] Although noble metals like platinum and rhodium exhibit high catalytic activity for the UOR, alternative catalysts that are both cost-effective and high-performance are highly required for large-scale systems. [9–11] Additionally, the development of a bifunctional electrocatalyst that can function as both an efficient anodic UOR catalyst and cathodic HER catalyst would streamline the system and reduce production costs. However, this remains a significant obstacle.

Nickel molybdate (NiMoO$_4$) has garnered significant attention as an active material for UOR applications due to its exceptional electrical conductivity of Mo and promising electrochemical activity arising from Ni. [12] However, intrinsic issues such as low electrical conductivity, sparse active sites, and poor durability impede its practical application. [13,14] To tackle the aforementioned challenges, doping with hetero-atoms offers a promising approach that can effectively modulate local electronic properties to enhance the electrochemical performance of materials. [15–17] Among the commonly utilized metallic species, chromium (Cr) stands out as a particularly appealing material for integration with NiMoO$_4$ due to its relatively low cost, abundant availability and diverse electronic structures. [18–20] In addition, the unique electrical confirmation of Cr^{3+} (t$_{2g}^3$e$_g^0$) contributes significantly to charge transfer and electronic trapping in electrocatalytic processes. [21–23] Furthermore, anionic surface modification is also a prevalent and efficient method for altering material surface properties, which can enhance catalytic activity, particularly when utilizing P doping as a valuable strategy to improve catalytic activity.[24,25] By modulating electronic structures in-situ with P atoms, intrinsic properties of host material remain unchanged. [26–28] In addition to improving the

* Corresponding author.
  E-mail address: rsong@ucas.ac.cn (R. Song).

intrinsic properties, doping is essential for shaping nanostructures by facilitating viable bond formation possibilities among similar and dissimilar elements. [29] Moreover, simultaneous doping of multiple elements holds the potential for fabricating superior nanostructures with enhanced surface area and electrochemically active sites. [30,31] Therefore, it can be inferred that co-doping and intercalation of various elements into $NiMoO_4$ will substantially boost its catalytic performance through enhancing the inherent properties such as conductivity, active site density on basal planes, generation of extra active sites, as well as physical characteristics like surface area.

Herein, we introduce a novel bifunctional electrocatalyst P/Cr dual-doped $NiMoO_4 \cdot 0.75\ H_2O$ (denoted as $P/Cr_{60}\text{-}NiMoO_4$) that features a distinctive structure of nanorod enveloped by nanosheets for energy-efficient urea-assisted H_2 production. Primarily, $Cr_x\text{-}NiMoO_4$ with a diversity of microstructures is successfully prepared by a facile hydrothermal process, where x represents the feeding of Cr element. Following by controlled phosphorization, the optimized $P/Cr_{60}\text{-}NiMoO_4$ catalyst shows excellent electrochemical performance for both HER and UOR processes. Furthermore, the coupled HER//UOR system in the two-electrode configuration exhibits an exceptional durability, i.e., delivering 100 mA cm^{-2} for over 60 h at an ultralow cell voltage of only 1.36 V. Theoretical calculations indicate that the incorporation of P and Cr atoms can facilitate charge redistribution, enhance conductivity, and significantly reduce the energy barrier for accelerating water dissociation. This work presents a novel method for fabricating highly active doped electrocatalysts, which can be utilized in energy-efficient hydrogen production and urea purification-based water splitting applications.

2. Experimental section

2.1. Synthesis of $Cr_x\text{-}NiMoO_4$

In a detailed procedure, add 435 mg of nickel nitrate hexahydrate ($Ni(NO_3)_2 \cdot 6\ H_2O$), 484 mg of sodium molybdate dihydrate ($Na_2MoO_4 \cdot 2\ H_2O$), and x mg of chromium chloride hexahydrate ($CrCl_3 \cdot 6\ H_2O$) in 30 mL of deionized water with vigorous stirring for 20 min. Then, transfer the resulting mixture with a piece of treated NF to a Teflon autoclave with a capacity of 50 mL. Finally, subject the

autoclave to treatment at a temperature of 160 °C for a duration of 6 h. After being cooled to room temperature, the surface was treated with deionized water and ethanol to eliminate any adsorbed impurities. Subsequently, it was dried under a vacuum atmosphere at 60 °C for 12 h. The doping concentration of Cr^{3+} ions varied from 0 mg to 80 mg in increments of 20 mg, and labeled as $Cr_x\text{-}NiMoO_4$, (X = 20 mg, 40 mg, 60 mg, 80 mg).

2.2. Synthesis of $P/Cr_x\text{-}NiMoO_4$

The $Cr_x\text{-}NiMoO_4$ and 1 g NaH_2PO_2 were placed in separate crucibles and transferred to the upstream and downstream of a tubular furnace, respectively. Subsequently, these substances were calcined at 350 °C for 2 h with a temperature ramp rate of 2 °C min^{-1} under an Ar atmosphere with a flow rate of 200 sccm in the tubular furnace to obtain $P/Cr_x\text{-}NiMoO_4$.

The materials characterizations and the parameters of electrochemical measurement are supplied in Supporting Information (SI).

3. Results and discussion

3.1. Synthesis and structural characterization

The synthetic strategy of the well-aligned P/Cr_{60}-doped $NiMoO_4$ catalytic materials is depicted in Fig. 1, where commercial nickel foam (NF) with a smooth surface is employed as conductive support owing to its excellent electrical conductivity and high surface area (Fig. S1). Initially, the well-designed $Cr_x\text{-}NiMoO_4$ samples with varying amounts of Cr doping are directly arranged on NF via a one-pot hydrothermal reaction. By adjusting the amount of Cr doping, the morphology and surface area of $NiMoO_4$ nanorods can be effectively tailored during the fabrication. The regulation of microstructure can promote electrolyte infiltration and expose more active sites, thereby augmenting the electrochemical properties. Afterward, the optimized $Cr_{60}\text{-}NiMoO_4$ that served as a precursor is converted into $P/Cr_{60}\text{-}NiMoO_4$ arrays with a controllable phosphorylation step. Accordingly, the color of $Cr_{60}\text{-}NiMoO_4$ also changes gradually from yellow-green to black (Fig. S2).

The evolutions of morphology and inner structure in the $P/Cr_x\text{-}NiMoO_4$ series are further monitored through scanning electron
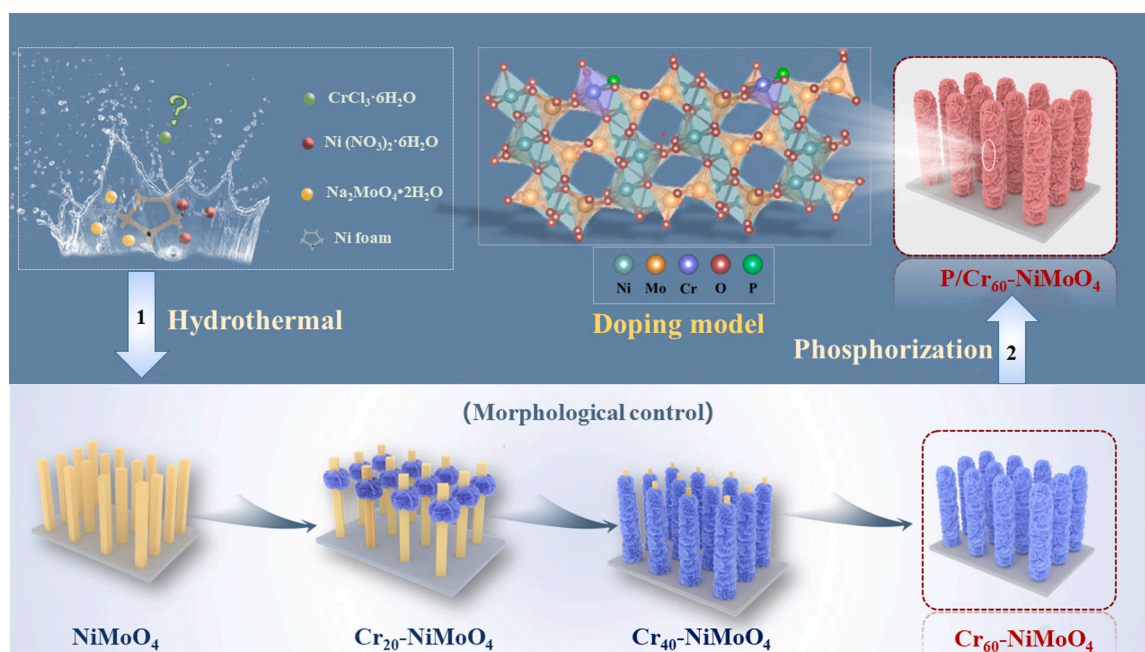

Fig. 1. Schematic illustration for the preparation of $P/Cr_{60}\text{-}NiMoO_4$.

microscopy (SEM) and transmission electron microscopy (TEM). The characteristic morphologies of $NiMoO_4$ with varying levels of Cr doping are shown in Fig. 2 and S3. In the absence of Cr source, a significant number of solid $NiMoO_4 \cdot nH_2O$ nanorods with smooth surfaces in an average diameter of about 200 nm are uniformly grown on NF surface (Fig. 2a). Upon introduction of Cr, Cr_{20}-$NiMoO_4$ exhibits a similar structure to $NiMoO_4$ while a few nanosheets are generated on the surface (Fig. 2b). With increasing of Cr content, a greater number of nanosheets are grafted onto the nanorod core, resulting in the formation of a tree-like nanoarray structure (Fig. 2c). Ultimately, with sufficient Cr doping, the nanorod core is almost completely surrounded by the nanosheets, forming an array structure resembling a cluster of flowers (Fig. 2d). The optimized Cr_{60}-$NiMoO_4$ nanoarray structure shows the largest surface area and tightest contact with the substrate, making it

highly favorable for electrochemical applications. Then, the Cr_{60}-$NiMoO_4$ precursor is identified as the optimal and used for subsequent analyses. After the thermal phosphorylation process, the obtained P/Cr_{60}-$NiMoO_4$ still shows a nanorod covered with numerous nanosheets (Fig. 2e-h, Figs. S4, 5). As shown in the high-resolution transmission electron microscopy (HRTEM) images (Fig. 2i-k), the P/Cr_{60}-$NiMoO_4$ exhibits clear lattice fringes with an interplanar spacing of 0.34 and 0.31 nm that correspond well to the (121) and (120) planes of $NiMoO_4$, indicating the composition of the P/Cr_{60}-$NiMoO_4$ nanostructure.[32] Meanwhile, the diffraction rings observed in the selective area electron diffraction (SAED) pattern of P/Cr_{60}-$NiMoO_4$ correspond to the facets of $NiMoO_4$ and are consistent with the from HRTEM results (Fig. 2l). The high-angle annular dark-field scanning transmission electron microscopy (HAADF-STEM) and corresponding elemental mapping images
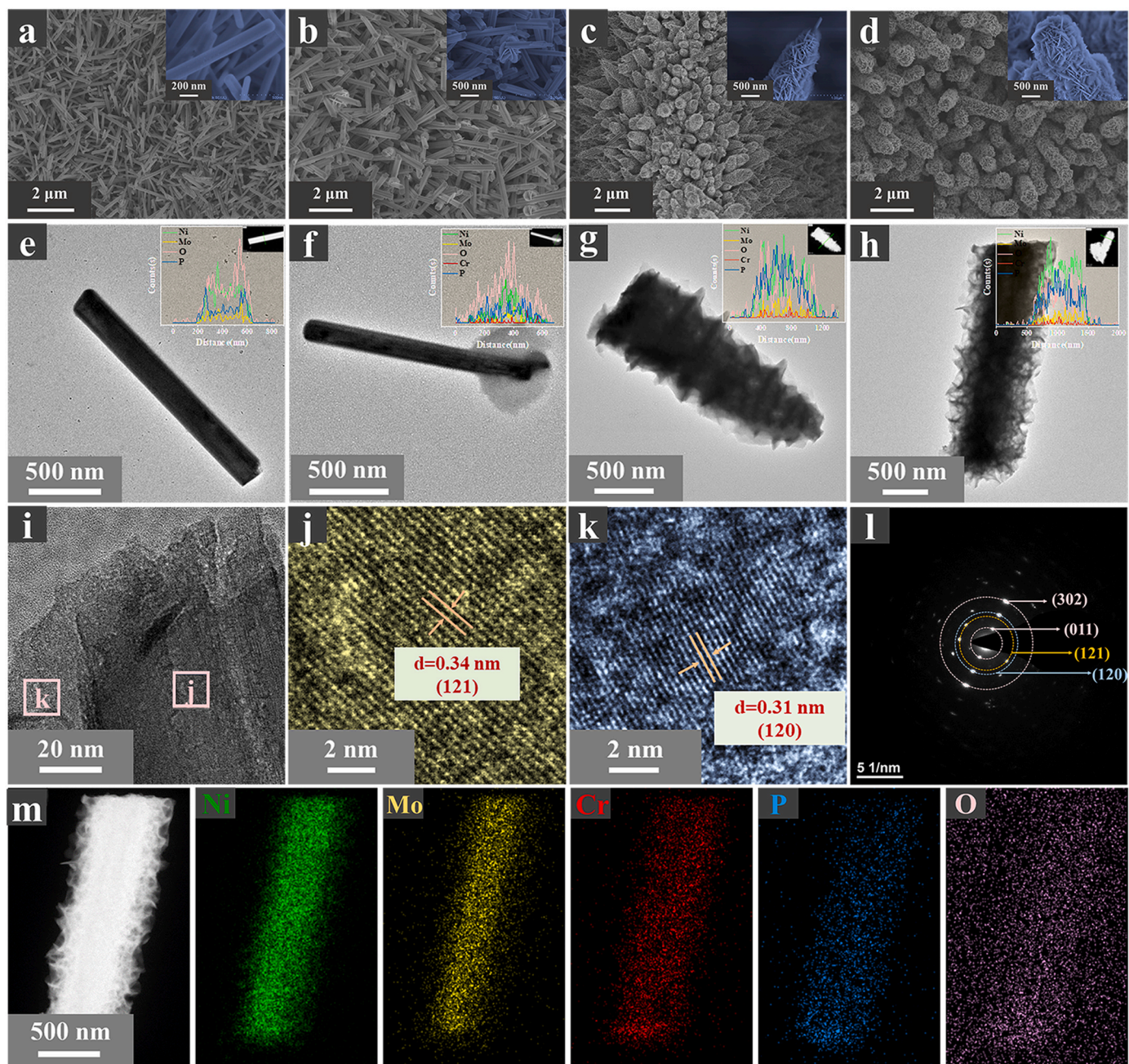

Fig. 2. SEM images with magnification for **a)** $NiMoO_4$, **b)** Cr_{20}-$NiMoO_4$, **c)** Cr_{40}-$NiMoO_4$, **d)** Cr_{60}-$NiMoO_4$. TEM images of **e)** P-$NiMoO_4$, **f)** P/Cr_{20}-$NiMoO_4$, **g)** P/Cr_{40}-$NiMoO_4$, **h)** P/Cr_{60}-$NiMoO_4$. **i)** TEM images, **j, k)** HRTEM images, and **l)** SAED pattern of P/Cr_{60}-$NiMoO_4$. **m)** HAADF-STEM image and the corresponding energy-dispersive X-ray spectroscopy elemental maps of P/Cr_{60}-$NiMoO_4$.

further verify the homogeneous distribution of Mo, Ni, Cr, P and O throughout the entire nanorod (Fig. 2m). In addition, the metal contents are determined by inductively coupled plasma atom emission spectrometry (ICP-AES). As shown in Table. S2, the contents of Ni, Mo, Cr and P for P/Cr$_{60}$-NiMoO$_4$ catalyst are 22.71 wt%, 30.27 wt%, 0.71 wt% and 8.74 wt%, respectively. The unique structure of nanorods wrapped by nanosheets is advantageous for increasing the contact area between the electrode and electrolyte, thereby enhancing the utilization of active sites.

The phase structure and chemical state of the prepared materials are analyzed via X-ray powder diffraction (XRD). Besides the three peaks belonging to metallic Ni (PDF #No.04–0850), the diffraction peaks observed in Fig. 3a for the Cr$_x$-NiMoO$_4$ sample can be attributed to hydrated NiMoO$_4$, which exhibits a triclinic crystal structure consistent with the simulated XRD patterns of NiMoO$_4$·0.75 H$_2$O. [33,34] Notably, the most intense diffraction peak at 13.43° of pure NiMoO$_4$·0.75 H$_2$O exhibits a noticeable negative shift in comparison with that of Cr$_x$-NiMoO$_4$ (Fig. S6), indicating the incorporation of Cr into the NiMoO$_4$. [21] As for P/Cr$_{60}$-NiMoO$_4$, no extra signals relating to P-based species can be detected, confirming the successful doping of P into the Cr$_x$-NiMoO$_4$ structure without the formation of new phases. However, it should be noted that the peak intensities for P/Cr$_{60}$-NiMoO$_4$ decrease with the P

doping, implying the depressed crystallinity. In addition, the structural characteristics are further analyzed via Raman spectroscopy. As depicted in Fig. 3b and S7, both Cr$_x$-NiMoO$_4$ and P/Cr$_{60}$-NiMoO$_4$ exhibit two vibrations of MoO$_4^{2-}$ (358 cm^{-1}) and Mo-O-Ni (800–1000 cm^{-1}), demonstrating the presence of similar surface oxides. [35,36] It is noteworthy that the Mo-O-Ni peaks also become weaker due to the introduction of P species, implying the oxide structure is destroyed, and this observation is in accord with the above XRD results.

The compositions, valence states and electronic interaction of NiMoO$_4$, Cr$_{60}$-NiMoO$_4$, and P/Cr$_{60}$-NiMoO$_4$ are further probed via X-ray photoelectron spectroscopy (XPS). The presence of Mo, Ni, Cr, P and O in P/Cr$_{60}$-NiMoO$_4$ are clearly verified (Fig. S8) and the atomic percentages revealed by XPS survey scan (Table S3). In the fine-scanned Ni 2p spectrum of P/Cr$_{60}$-NiMoO$_4$, the peaks observed at 856.91 and 880.10 eV, accompanied by two shakeup satellites (861.71 eV and 874.72 eV), can be attributed to Ni^{2+} 2p$_{3/2}$ and Ni^{2+} 2p$_{1/2}$, while the peak located at 852.97 eV corresponds to metallic Ni (Fig. 3c). [31,37] The Mo 3d peaks at 232.32 and 235.45 eV for Mo^{6+} in the Cr$_{60}$-NiMoO$_4$ display a negligible positive shift in comparison to NiMoO$_4$, suggesting that the presence of Cr dopants has an impact on the electronic structure of Mo atoms (Fig. 3d). [38] In contrast, the Mo related peaks in P/Cr$_{60}$-NiMoO$_4$ can be deconvoluted into two components of Mo^{4+}
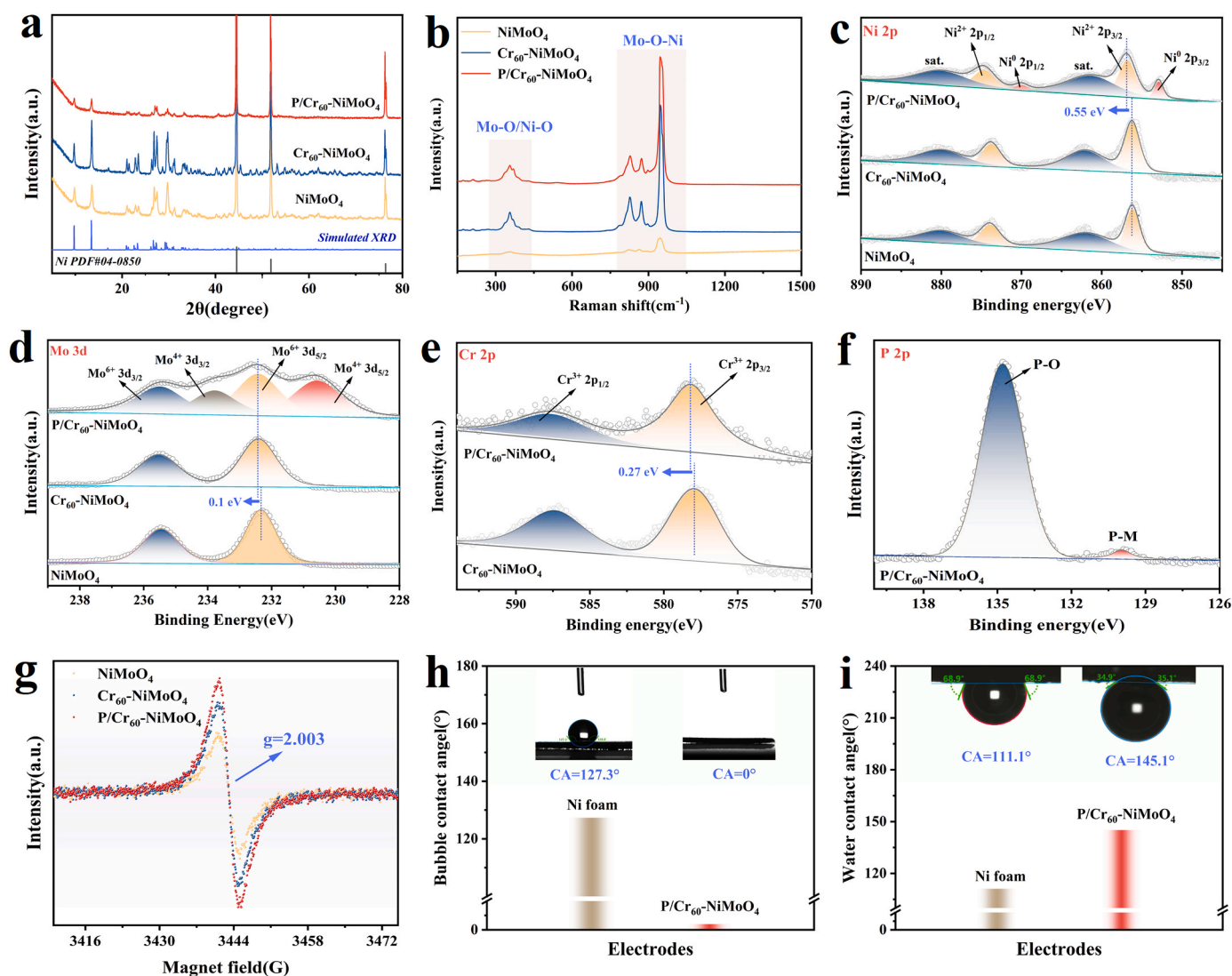

Fig. 3. a) XRD patterns, **b)** Raman spectra, **c)** High-resolution Ni 2p XPS spectra and **d)** high-resolution Mo 3d XPS spectra of NiMoO$_4$, Cr$_{60}$-NiMoO$_4$ and P/Cr$_{60}$-NiMoO$_4$. **e)** High-resolution Cr 2p XPS spectra of NiMoO$_4$ and Cr$_{60}$-NiMoO$_4$. **f)** High-resolution P 2p XPS spectra of P/Cr$_{60}$-NiMoO$_4$. **g)** EPR spectra of NiMoO$_4$, Cr$_{60}$-NiMoO$_4$ and P/Cr$_{60}$-NiMoO$_4$. **h)** Water CAs and **i)** underwater gas-bubble CAs of P/Cr$_{60}$-NiMoO$_4$.

(232.32 and 235.45 eV) and Mo^{6+} (230.57 and 233.79 eV), respectively, which are ascribed to the partial reduction of Mo^{6+} during the phosphorylation treatment process. [39] In Cr 2p spectrum, the core-level spectrum could be matched with the two singles that represent peaks of Cr $2p_{1/2}$ and Cr $2p_{3/2}$ for Cr^{3+}, implying that the metal ions contained in the P/Cr_{60}-NiMoO$_4$ inherit the original valence state from the raw reagent (Fig. 3e). [40] In addition, the 129.97 eV peak in the high-resolution P 2p spectra is stemmed from P-metal bonds in P/Cr_{60}-NiMoO$_4$ (Fig. 3f), and the second 134.77 eV peak can be attributed to the P-O band resulting from the unavoidable exposure to air. [41] The O 1 s spectrum (Fig. S9) can be deconvoluted into three distinctive peaks corresponding to metal-O bond (M-O), oxygen vacancy (O_V), and adsorbed water molecular (O_{ads}) at binding energies of 530.48, 531.52, and 533.06 eV, respectively. Notably, the introduction of P doping results in a positive shift in the binding energy of Ni 2p due to the stronger electronegativity relative to Ni, leading to a reduction in electron concentration surrounding Ni 2p. Thus, it is discovered that inserting P element alters the electronic structure of Cr_{60}-NiMoO$_4$, potentially resulting in a better catalytic property. Besides, the incorporation of Cr atoms with varying atomic radii and coordination configurations also results in the enrichment of O_v, as evidenced by the electron paramagnetic resonance (EPR) spectra (Fig. 3g). [42] As indicated, the EPR spectrum of Cr_{60}-NiMoO$_4$ displays a pronounced signal at g = 2.003, which is indicative of O_v and more intense than that observed in NiMoO$_4$. [43] The characteristic signal of enhanced O_v in P/Cr_{60}-NiMoO$_4$ is also detected compared with Cr_{60}-NiMoO$_4$, suggesting that the phosphorization process also increases the concentration of O_v in NiMoO$_4$. Generally, O_v is widely recognized as essential oxygen carriers and active sites for oxygen intermediates during the UOR process.[44].

The surface property is noticeable in assessing the electrocatalyst. In this case, the wettability and aerophobicity P/Cr_{60}-NiMoO$_4$ is evaluated through contact angle (CA) measurements with water and underwater gas bubbles (Figs. 3h, 3i). [45] The gas bubble contact angle in the air of P/Cr_{60}-NiMoO$_4$ and NF are 0° and 127.3°, respectively, demonstrating the super-hydrophilic nature of P/Cr_{60}-NiMoO$_4$ that benefits contact between the electrolyte and electrode. Besides, the contact angles under water of P/Cr_{60}-NiMoO$_4$ and NF are 145.1° and 111.1°, respectively, indicating the outstanding aerophobicity of P/Cr_{60}-NiMoO$_4$. The exceptional aerophobicity will enhance the reaction kinetics by
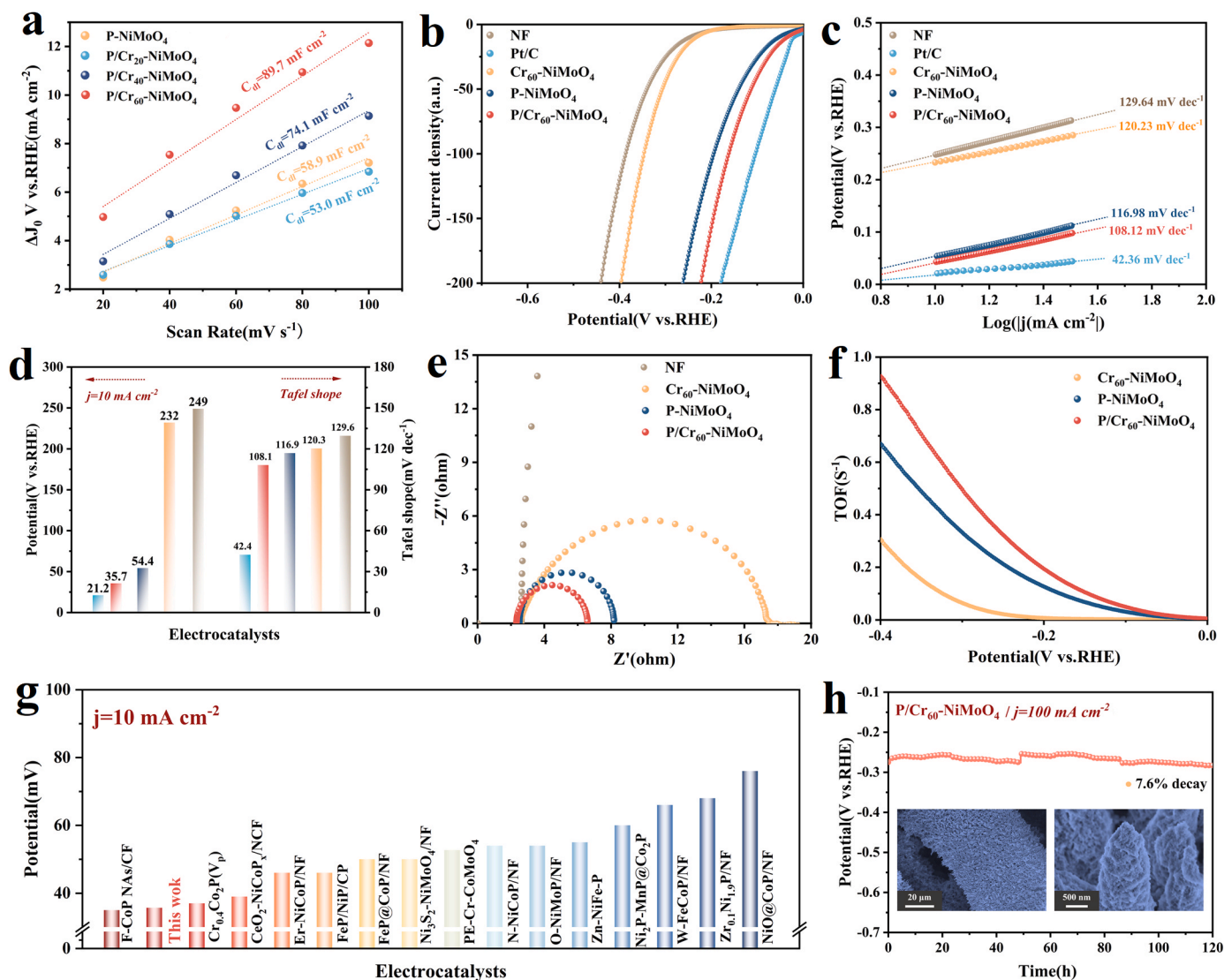

Fig. 4. a) Influence of Cr doping on C_{dl} for P/Cr_x-NiMoO$_4$. **b)** Linear sweep voltammetry (LSV) curves and **c)** Tafel plots of NF, Pt/C, Cr_{60}-NiMoO$_4$, P-NiMoO$_4$ and P/Cr_{60}-NiMoO$_4$ in 1 M KOH. **d)** Comparison of overpotentials at 10 mA cm^{-2} and Tafel plots of different catalysts. **e)** Nyquist plots and **f)** TOF value of Cr_{60}-NiMoO$_4$, P-NiMoO$_4$ and P/Cr_{60}-NiMoO$_4$. **g)** Comparison of the overpotentials for some recently reported electrocatalysts at 10 mA cm^{-2}. **h)** Chronopotentiometry measurements at 100 mA cm^{-2} for P/Cr_{60}-NiMoO$_4$ without iR compensation (inset: SEM images of P/Cr_{60}-NiMoO$_4$ after HER test in 1 M KOH).

facilitating rapid detachment of bubbles from the surface of the electrocatalyst, thereby promoting the continuous engagement between active sites and electrolytes. Collectively, the superior wettability and aerophobicity of P/Cr$_{60}$-NiMoO$_4$ can facilitate reactant diffusion, including local electrolyte recovery and bubble separation, which are critical for industrial electrocatalytic reactions at high current densities. [46].

3.2. Electrochemical HER activities

The electrochemical surface areas (ECSAs) of the P/Cr$_x$-NiMoO$_4$ are determined by capacitance measurements using cyclic voltammetry at various scan rates, in the double-layer region where no faradaic processes occur (Fig. S10). As illustrated in Fig. 4a, the increasing Cr loading raises the C$_{dl}$ from 53.0 mF cm^{-2} for P-NiMoO$_4$ to 89.7 mF cm^{-2} for P/Cr$_{60}$-NiMoO$_4$. This result indicates that the Cr doping is a feasible way to modulate the ECSAs of P/Cr$_x$-NiMoO$_4$ (Fig. S11). Moreover, the C$_{dl}$ value of P/Cr$_{60}$-NiMoO$_4$ is much higher than Cr$_{60}$-NiMoO$_4$ (58.9 mF cm^{-2}), demonstrating that P/Cr$_{60}$-NiMoO$_4$ has the highest density of active sites for HER (Fig. S12). Consequently, the P/Cr$_{60}$-NiMoO$_4$ has the best electrochemical activity (Fig. S13). The HER property of the optimal and other comparative samples is further evaluated, and the corresponding curves without iR-compensation are shown in Fig. S14. The polarization curves in Fig. 4b show that P/Cr$_{60}$-NiMoO$_4$ holds an overpotential of 35.7 mV at the current density of 10 mA cm^{-2}, drastically lower than that of P-NiMoO$_4$ (54.4 mV), Cr$_{60}$-NiMoO$_4$ (232 mV), and NF (240 mV). Further, the Tafel plots derived from LSV curves are presented in Fig. 4c. Impressively, the Tafel slope of P/Cr$_{60}$-NiMoO$_4$ only overtops that of Pt/C, but significantly lower than that of other catalysts, indicating the faster reaction kinetics of P/Cr$_{60}$-NiMoO$_4$ (Fig. 4d). [47] Electrochemical impedance spectroscopy (EIS) is employed to analyze the charge transfer characteristics of the catalysts. As depicted in Fig. 4e, the P/Cr$_{60}$-NiMoO$_4$ exhibits a significantly lower charge transfer resistance of 6.2 Ω than that of P-NiMoO$_4$ (8.1 Ω), Cr$_{60}$-NiMoO$_4$ (17.8 Ω), and NF (43.3 Ω), implying its superior electrical conductivity and faster electron-transfer kinetics, which greatly contribute to the enhanced HER activity. [48] Turnover frequency (TOF) is widely recognized as a reliable indicator of intrinsic catalytic activity (Fig. S15). [45] The interfacial P/Cr-doping significantly enhances the intrinsic activity towards HER, as evidenced by the highest TOF values for the P/Cr$_{60}$-NiMoO$_4$ (Fig. 4f). Finally, the electrochemical stability of the P/Cr$_{60}$-NiMoO$_4$ electrode towards HER is confirmed by its high current retention (92.3%) after continuous operation for 120 h at a current density of 100 mA cm^{-2} (Fig. 4h). These results indicate that P/Cr$_{60}$-NiMoO$_4$ has good stability and catalytic activity, outperforming previous reported comparable catalysts, as summarized in Fig. 4g and Table S5.

To gain a deeper understanding of the changes in P/Cr$_{60}$-NiMoO$_4$ after stability testing, we conduct further analysis on the surface elements and morphology post-testing. The SEM images show that the nanoarrays are nearly intact, verifying the remarkable stability of the P/Cr$_{60}$-NiMoO$_4$ (inset in Fig. 4h). In addition, the presence of Ni, Mo, Cr, P and O is confirmed by EDX spectra (Fig. S16) and XPS survey spectrum (Fig. S17a). The post-mortem XPS analysis shows that the signal related to Ni^0 was not observed in Fig. S17b, implying the surface oxidization of P/Cr$_{60}$-NiMoO$_4$ during HER. [49] Notable, the trivalent state of Cr (Cr^{3+}) remains predominant with negligible alteration (Fig. S17d), while the hexavalent form of Mo (Mo^{6+}) is predominantly present due to the oxidation of exposed Mo by OH$^-$ in the alkaline media. [50] In contrast, the M-O peak remains unchanged while the O-H peak noticeably decreases post-reaction, which is attributed to the reduction in surface area and subsequent decrease in the available adsorption sites. (Fig. S17e). Based on the significantly enhanced PO$_4^{3-}$ peak observed in the P 2p spectrum, we hypothesize that insoluble metal phosphate is formed on its surface (Fig. S17f). [51] Furthermore, the XRD analysis (Fig. S18) reveals that there is no significant difference in the phase

change of post-HER P/Cr$_{60}$-NiMoO$_4$ compared with the original catalyst, manifesting that the superior HER stability of the electrode could be attributed to the intrinsic properties of P/Cr$_{60}$-NiMoO$_4$.

3.3. Electrochemical UOR activities

Given that concentration of urea in human urine is ca. 2–2.5 wt% ($\approx$ 0.33 M), the electrochemical catalytic properties of the as-prepared catalysts are evaluated in 1 M KOH with 0.33 M urea. As shown in Fig. 5a, The P/Cr$_{60}$-NiMoO$_4$ catalyst shows a low onset potential of 1.32 V for the electrocatalytic UOR and a high current density of 100 mA cm^{-2} is achieved at overpotential of only 1.36 V, about 270 mV reduced to gain the same current density as compared to the OER performed in 1 M KOH. The UOR activity of P/Cr$_{60}$-NiMoO$_4$ is optimized at 1 M KOM with 0.33 M urea, while the influence of scan rates on the performance is also investigated (Fig. S20). The activity is evaluated by LSV test, and the results indicated that P/Cr$_{60}$-NiMoO$_4$ exhibited superior performance comparing with other samples (Fig. 5b and S19). Moreover, the Tafel slopes are calculated in order to elucidate the kinetics of UOR. As expected, the P/Cr$_{60}$-NiMoO$_4$ shows a substantially lower Tafel slope (31.95 mV dec^{-1}), surpassing that of P-NiMoO$_4$ (41.68 mV dec^{-1}), Cr$_{60}$-NiMoO$_4$ (73.28 mV dec^{-1}) and NF (78.28 mV dec^{-1}), thus evidencing its favorable kinetics (Fig. 5c, d). The above results prove that the P/Cr$_{60}$-NiMoO$_4$ assumes superior activity, which ranks among the best-reported urea electrocatalysis systems (Table S6).

The interfacial behaviors of P/Cr$_{60}$-NiMoO$_4$ in various electrolyte solutions are investigated by operando EIS test. When the applied potential surpasses 1.38 V vs. RHE in 1 M KOH (Fig. 5e, g), both the diameter of the semicircle and phase angle at low-frequency regions decrease, demonstrating an occurrence of OER process and a reduction in charge transport resistance with rising applied potential. [2] In 1 M KOH with 0.33 M urea, the Nyquist plots exhibit almost linear distribution and the Bode plots show no arched phase angle when the potential is raised to 1.28 V vs. RHE, indicating the absence of interfacial charge transfer within this potential range (Fig. 5f, h). [52] As the potential increase, the arched phase angle at the low-frequency region appears at 1.3 V vs. RHE along with a well-defined semicircle in the Nyquist plot, which suggests the initiation of interfacial charge transfer related to UOR at this potential. This observation is in line with the phenomenen that the onset current of UOR falls within the potential range of 1.30 V vs. RHE, and an increase in potential from 1.30 to 1.38 V vs. RHE leads to a reduction in phase angles and charge transport resistance. Furthermore, the addition of urea results in a significant decrease in peak phase angle at low potential compared to the OER, indicating a reduction in the driving potential required for interfacial charge transfer associated with the UOR process (Fig. S21). [53]

Besides the excellent UOR activity, the electrochemical stability of P/Cr$_{60}$-NiMoO$_4$ is further assessed with chronopotentiometry. As shown in Fig. 5i, the potential change is negligible during 60 h of electrolysis at a current density of 100 mA cm^{-2}, manifesting the admirable durability towards UOR. To uncover the origin of the high stability, post-catalytic analyses are conducted using a series of experimental characterizations. The morphology of this electrode is well preserved even after long-term electrochemical tests, verifying the remarkable mechanical robustness (SEM images, inset in Fig. 5i). In the high-resolution XPS spectra of Ni 2p, the absence of a signal related to Ni^0 in Fig. S22b suggests that the catalyst surface has undergone oxidation. [14] The peak intensity of Mo 3d in Fig. S22c and P 2p in Fig. S22e exhibits a significant reduction, indicating the inevitable loss of MoO$_4^{2-}$ and PO^{4-} during the stability test. Notably, no significant changes occur in the spectrum of Cr 2p (Fig. S22d). In the O 1 s spectra (Fig. S22f), the intensities of M-O peaks decrease while that of O$_v$ increases, indicating a gradual disappearance of metal-oxygen bonds during urea electrolysis and the formation of O$_v$. To further identify the active phase and dynamic surface reconstruction of P/Cr$_{60}$-NiMoO$_4$, in-situ Raman spectroscopy is conducted in 1 M KOH as a function of applied potential at intervals of 0.1 V (Fig. S23a). The
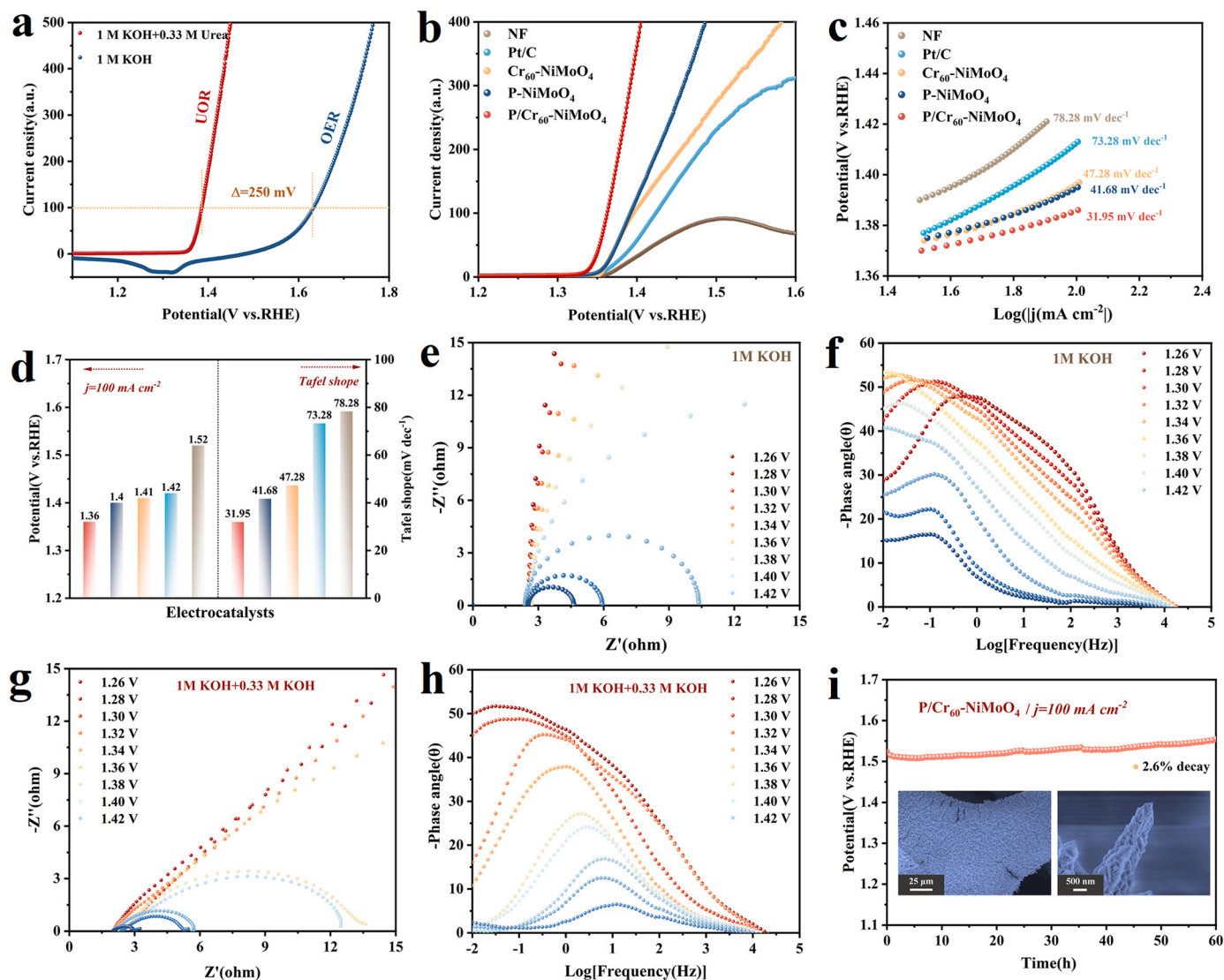
Fig. 5. a) Polarization curves of P/Cr$_{60}$-NiMoO$_4$ in 1 M KOH with and without 0.33 M urea. **b)** UOR polarization curves and **c)** Tafel plots of NF, RuO$_2$/NF, Cr$_{60}$-NiMoO$_4$, P-NiMoO$_4$ and P/Cr$_{60}$-NiMoO$_4$ in 1 M KOH containing 0.33 M urea. **d)** Comparison of potentials at 10 mA cm^{-2} and Tafel plots of different catalysts. Operando EIS measurements: **e, g)** Nyquist plots and **f, h)** Bode-phase plots collected under different anodic polarization potentials for P/Cr$_{60}$-NiMoO$_4$ in 1 M KOH without and with 0.33 M urea, respectively. **i)** Chronopotentiometry measurements at 100 mA cm^{-2} for P/Cr$_{60}$-NiMoO$_4$ without iR compensation (inset: SEM images of P/Cr$_{60}$-NiMoO$_4$ after UOR test).

Raman spectra exhibit no discernible variation when the potential input is below 1.4 V vs. RHE. As the potential rises to 1.4 V vs. RHE, M-OOH begins to emerge and dominates the surface of the P/Cr$_{60}$-NiMoO$_4$, as demonstrated by the intensities of the representative vibrational modes (475 and 554 cm^{-1}), which increase rapidly with rising potential. After the cessation of potential, the reconstructed surface retains the trivalent Ni motifs (NiOOH), indicating that this phase is stable. Regarding the in situ Raman tests in UOR, the reconstructed P/Cr$_{60}$-NiMoO$_4$ is initially electrochemically oxidized into an active-phase NiOOH, which is subsequently reduced to the Ni^{2+} state by urea deprotonation. During this process, OH$^-$ in NiOOH reacts with H$^-$ of urea to form a water molecule, thus initiating the catalytic cycle again. [54] As a result of the fast UOR kinetics of P/Cr$_{60}$-NiMoO$_4$, the newly produced Ni^{3+} is swiftly devoured by urea before it can be detected by Raman test, resulting in the absence of NiOOH signal (Fig. S23c).

3.4. Catalytic activity toward overall electrolysis

Given the excellent bifunctional electrocatalytic activity towards both UOR and HER, a hydrogen production device with energy-saving properties is assembled using the P/Cr$_{60}$-NiMoO$_4$ as two electrodes (Fig. 6a, Fig. S24). As experimentally proved that in Fig. 6b, the urea-aided water electrolysis has a more favorable overall performances including lower cell voltage and reduced energy consumption. In particular, the P/Cr$_{60}$-NiMoO$_4$ displays lower cell voltages of only 1.35, 1.46, and 1.50 V, respectively, for achieving overall urea splitting current densities of 10, 50, and 100 mA cm^{-2} (Fig. 6c). In contrast, the commercial catalysts Pt/C//RuO$_2$ exhibits a higher potential (1.54 V @ 10 mA cm^{-2}) (Fig. S25). The excellent long-term stability of P/Cr$_{60}$-NiMoO$_4$ couple embodies a negligible activity decay under high current densities of 100 mA cm^{-2} (3.7%) for 60 h (Fig. 6d). In addition, the Faradaic efficiency and hydrogen production rate are calculated to be 98.2% and 1.34 mmol h^{-1}, respectively, demonstrating the enormous potential of P/Cr$_{60}$-NiMoO$_4$ (Fig. S26 and 27). Moreover, the two-electrode system can be powered by a 1.50 V battery and the electrode-generated bubbles are clearly visible (Fig. 6e). Remarkably, P/Cr$_{60}$-NiMoO$_4$ outperforms most recently developed electrocatalysts in terms of urea electrolysis performance (Fig. 6f). Based on these comprehensive
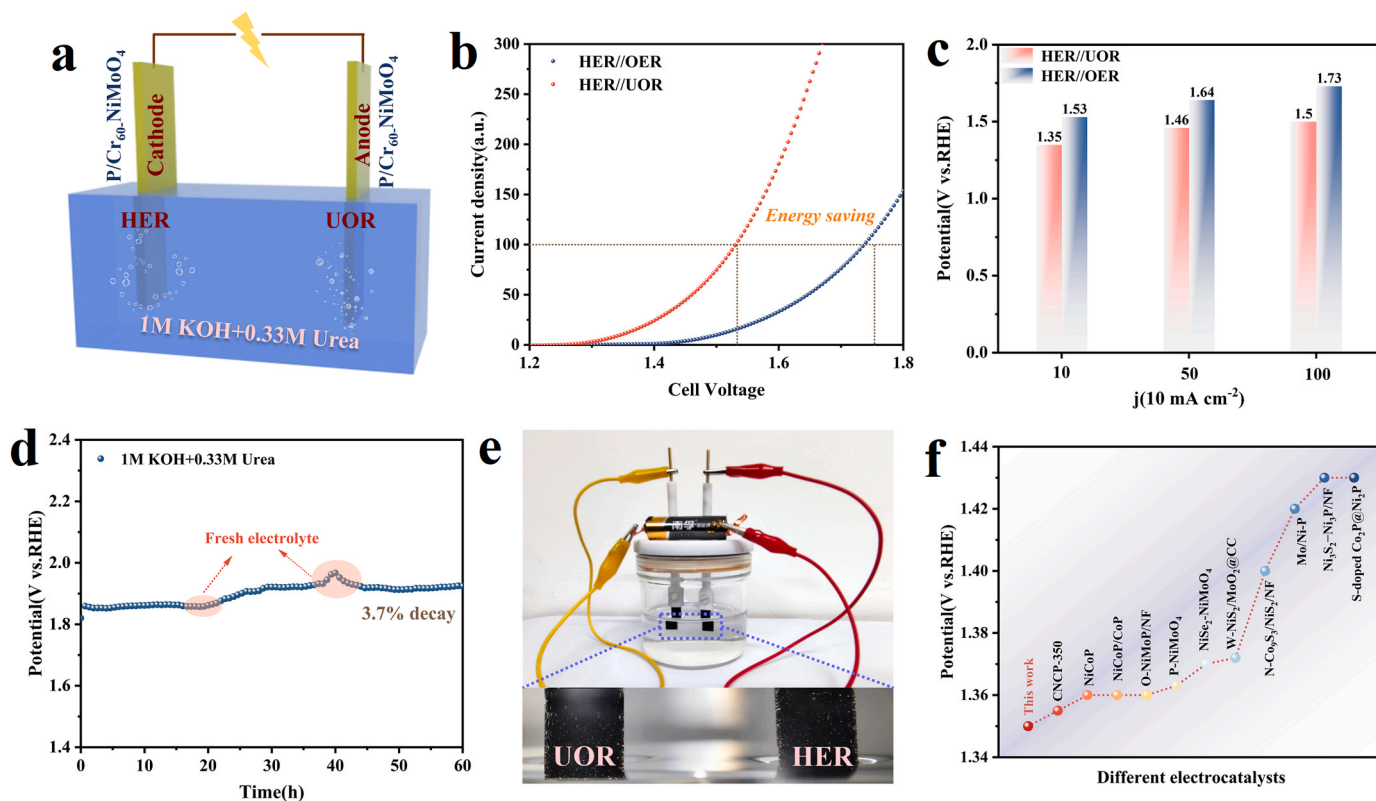
Fig. 6. a) The schematic plot showing the urea electrolyzer using P/Cr$_{60}$-NiMoO$_4$ as the anode and cathode. **b)** Comparison of the LSV curves for P/Cr$_{60}$-NiMoO$_4$ in urea electrolysis and water splitting. **c)** Comparison of cell voltage in different coupled systems. **d)** Cell stability test of P/Cr$_{60}$-NiMoO$_4$ in the configuration of HER// UOR. **e)** Optical photograph of a water splitting device based on P/Cr$_{60}$-NiMoO$_4$ powered by a battery with a nominal voltage of 1.5 V. **f)** Activity compared with other electrocatalysts.

advantages, P/Cr$_{60}$-NiMoO$_4$ can be considered a promising self-supporting electrode for energy-efficient hydrogen production.

3.5. DFT calculations

Density functional theory (DFT) calculations are performed to obtain the deep insights about the reaction mechanisms of UOR and HER at the anode and cathode. The calculation models are constructed based on the analysis of XRD and TEM results. The (121) plane of NiMoO$_4$·0.75 H$_2$O is selected as the reaction surface (Fig. 7a). Additionally, the surface metal and O atoms are replaced to simulate the doping phenomenon (Fig. 7b). To uncover the mechanism for the performance improvement, the charge density difference of the urea adsorption process and the bonding states in the intermediate model are calculated. As depicted in Fig. 7c, electron transfer from the urea molecule to metal-O and N-C bonds, thus the molecule is activated and further promotes the dehydrogenation reaction. Notably, the urea molecule on the surface of P/Cr$_{60}$-NiMoO$_4$ exhibits a significantly larger charge deficiency region as compared to that on the surface of NiMoO$_4$, thereby enabling a higher degree of activation for urea molecules in the doping system. Then, the free energy of UOR processes on the active sites of NiMoO$_4$·nH$_2$O and P/Cr$_{60}$-NiMoO$_4$ are calculated (Fig. S28). As shown in Fig. 7e, the thermodynamic analysis indicates that urea molecules can be adsorbed stably onto both P/Cr$_{60}$-NiMoO$_4$ (121) and P/Cr$_{60}$-NiMoO$_4$ (121) surfaces. Particularly, the P/Cr$_{60}$-NiMoO$_4$ (121) presents a lower adsorption-free energy (ΔG_{urea}), indicating a stronger interaction between the catalyst and the intermediate. The following dehydrogenation steps (*CONH$_2$NH$_2$→*CONNH) show a continuous increase in the energy trend. For NiMoO$_4$ and P/Cr$_{60}$-NiMoO$_4$, the potential determining steps (PDSs) locate at the first (*CONH$_2$NH$_2$→*CONHNH$_2$) and last (*CONNH→*CON$_2$) dehydrogenation steps, respectively, with

maximum free energy change (ΔG_{max}) of 2.78 eV and 1.62 eV. Therefore, the catalytic performance is significantly improved through the doping process. Furthermore, the crystal orbital Hamilton population (COHP) calculations show that no antibonding is observed for the C-O bond in the UOR on the surface of NiMoO$_4$, while an antibonding peak is found under the Fermi energy for the C-N bond, which weakens the stable bonds in the urea molecule and benefits for the dehydrogenation process (Fig. 7f). Particularly, the antibonding states of C-N bond shift to lower energy levels after P and Cr co-doping, thus the activation degree of urea molecule is enhanced. On the other side, the HER performance is evaluated by the free energy calculations of the H$_2$ forming process through the combination of protons (Fig. 7g). The adsorption-free energy of proton ($\Delta G(H^*)$) is 2.46 eV for NiMoO$_4$, which reduces to −0.18 eV at the Ni-P site after the doping of Cr and P. Hence, the HER catalytic ability is effectively improved. Besides, the density of states (DOS) presents a significant band gap for the pristine NiMoO$_4$·nH$_2$O, while more electronic states occur at the Fermi energy for the P/Cr$_{60}$-NiMoO$_4$ unitcell, indicating that the conductivity of the catalyst is improved by the co-doping of Cr and P. In short, the catalytic performance is significantly enhanced (Fig. 7h).

4. Conclusion

In summary, a highly efficient and durable bifunctional catalyst for both HER and UOR has been synthesized by integrating P and Cr co-doped NiMoO$_4$·0.75 H$_2$O. The P/Cr$_{60}$-NiMoO$_4$ electrode exhibits high conductivity and an enlarged electrochemical surface area, resulting in enhanced activity, rapid mass/charge transport, the facile release of generated gas bubbles, and favorable stability for electrocatalytic processes. Therefore, when utilized in water electrolysis, the P/Cr$_{60}$-NiMoO$_4$ catalyst exhibits exceptional catalytic activities for both UOR
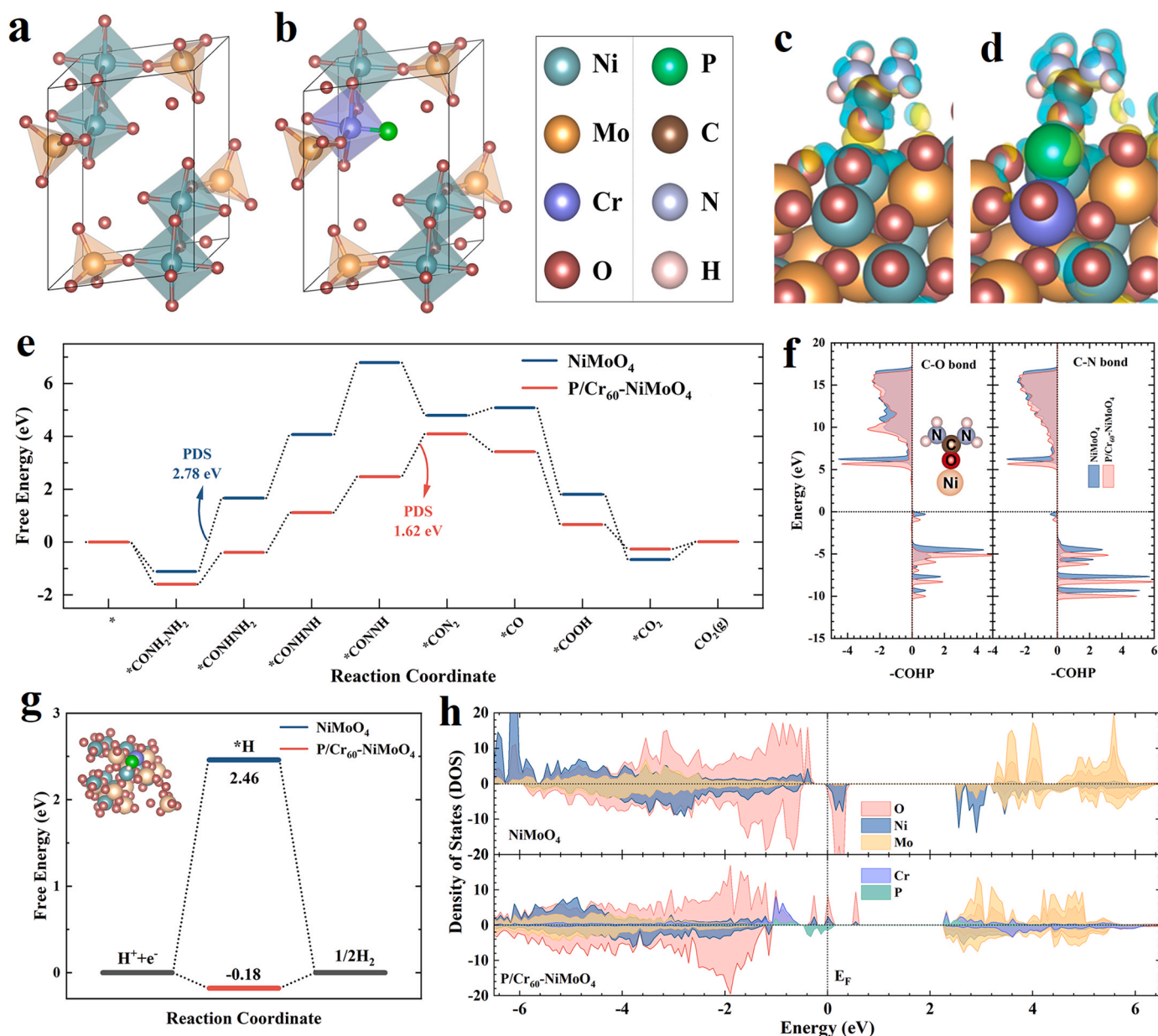
Fig. 7. Atomic structure models for **a)** $NiMoO_4$ and **b)** P/Cr_{60}-$NiMoO_4$. The charge density difference profiles of the Urea molecule adsorbed on the **c)** $NiMoO_4$ (121) and **d)** P/Cr_{60}-$NiMoO_4$ (121) surfaces. **e)** The free energy diagram of UOR process on the $NiMoO_4$ (121) and P/Cr_{60}-$NiMoO_4$ (121) surfaces. **f)** The COHP of the metal-O, C-O, and C-N bonds in the urea adsorption models. **g)** The free energy profile of HER process on the $NiMoO_4$ (121) and P/Cr_{60}-$NiMoO_4$ (121) surfaces. **h)** The density of states (DOS) of the pristine and P/Cr_{60}-$NiMoO_4$ unit cell.

and HER reactions in alkaline media, indicating its great potential for practical applications in overall urea splitting. Theoretical calculations indicate that P/Cr_{60}-$NiMoO_4$ exhibits a low dissociation barrier for H_2O and an close-to-zero adsorption-free energy for the H intermediate, those are conducive to the HER process. Furthermore, optimization of the electronic structure in the co-doping system alters the potential-determining step of UOR and effectively reduces its potential barrier, thereby promoting the UOR process. This study highlights the significant enhancement of catalytic activity towards both UOR and HER through the P/Cr cooperation, which provides a promising avenue for developing high-performance catalysts in energy-efficient hydrogen production.

CRediT authorship contribution statement

Yanyan Li: Conceptualization, Methodology, Investigation, Formal analysis, Project administration, Writing – original draft. **Haoran Guo**: Investigation, Software. **Yao Zhang**: Investigation. **Rui Song**: Materials characterization, Resources, Supervision, Funding acquisition.

Declaration of Competing Interest

The authors declare that they have no known competing financial interests or personal relationships that could have appeared to influence the work reported in this paper.

Data availability

Data will be made available on request.

Acknowledgment

Appendix A. Supporting information

Supplementary data associated with this article can be found in the online version at doi:10.1016/j.apcatb.2023.123296.

References

[1] S.K. Geng, Y. Zheng, S.Q. Li, H. Su, X. Zhao, J. Hu, H.B. Shu, M. Jaroniec, P. Chen, Q.H. Liu, Nickel ferrocyanide as a high-performance urea oxidation electrocatalyst, Nat. Energy 6 (2021) 904–912, https://doi.org/10.1038/s41560-021-00899-2.

[2] J. Li, J. Li, T. Liu, L. Chen, Y. Li, H. Wang, X. Chen, M. Gong, Z.P. Liu, X. Yang, Deciphering and suppressing over-oxidized nitrogen in nickel-catalyzed urea electrolysis, Angew. Chem. Int. Ed. 133 (2021) 26860–26866, https://doi.org/10.1002/anie.202114404.

[3] L. Wang, Y. Zhu, Y. Wen, S. Li, C. Cui, F. Ni, Y. Liu, H. Lin, Y. Li, H. Peng, Regulating the local charge distribution of Ni active sites for the urea oxidation reaction, Angew. Chem. 133 (2021) 10671–10676, https://doi.org/10.1002/anie.202010610.

[4] P. Wang, X. Bai, H. Jin, X. Gao, K. Davey, Y. Zheng, Y. Jiao, S.Z. Qiao, Directed urea-to-nitrite electrooxidation via tuning intermediate adsorption on Co, Ge Co-doped Ni sites, Adv. Funct. Mater. (2023), 2300687, https://doi.org/10.1002/adfm.202300687.

[5] J. Zhang, X. Song, L. Kang, J. Zhu, L. Liu, Q. Zhang, D.J. Brett, P.R. Shearing, L. Mai, I. Parkin, Stabilizing efficient structures of superwetting electrocatalysts for enhanced urea oxidation reactions, J. Chem. Catal. 2 (2022) 3254–3270, https://doi.org/10.1016/j.checat.2022.09.023.

[6] M.P. Browne, Z. Sofer, M. Pumera, Layered and two dimensional metal oxides for electrochemical energy conversion, Energy Environ. Sci. 12 (2019) 41–58, https://doi.org/10.1039/C8EE02495B.

[7] H. Jiang, M. Sun, S. Wu, B. Huang, C.S. Lee, W. Zhang, Oxygen-incorporated NiMoP nanotube arrays as efficient bifunctional electrocatalysts for urea-assisted energy-saving hydrogen production in alkaline electrolyte, Adv. Funct. Mater. 31 (2021), 2104951, https://doi.org/10.1002/adfm.202104951.

[8] X. Zheng, J. Yang, P. Li, Z. Jiang, P. Zhu, Q. Wang, J. Wu, E. Zhang, W. Sun, S. Dou, Dual-atom support boosts nickel-catalyzed urea electrooxidation, Angew. Chem. Int. Ed. (2023), e202217449, https://doi.org/10.1002/anie.202217449.

[9] J. Jin, J. Yin, H. Liu, B. Huang, Y. Hu, H. Zhang, M. Sun, Y. Peng, P. Xi, C. Yan, Atomic sulfur filling oxygen vacancies optimizes H absorption and boosts the hydrogen evolution reaction in alkaline media, Angew. Chem. Int. Ed. 133 (2021) 14236–14242, https://doi.org/10.1002/anie.202104055.

[10] H. Yu, S. Zhu, Y. Hao, Y. Chang, L. Li, J. Ma, H. Chen, M. Shao, S. Peng, Modulating local interfacial bonding environment of heterostructures for energy-saving hydrogen production at high current densities, Adv. Funct. Mater. (2023), 2212811, https://doi.org/10.1002/adfm.202212811.

[11] T. Wang, X. Cao, L. Jiao, Progress in hydrogen production coupled with electrochemical oxidation of small molecules, Angew. Chem. Int. Ed. (2022), e202213328, https://doi.org/10.1002/anie.202213328.

[12] D. Guo, Y. Luo, X. Yu, Q. Li, T. Wang, High performance NiMoO4 nanowires supported on carbon cloth as advanced electrodes for symmetric supercapacitors, Nano Energy 8 (2014) 174–182, https://doi.org/10.1016/j.nanoen.2014.06.002.

[13] P. Sharma, M. Minakshi, J. Whale, A. Jean-Fulcrand, G. Garnweitner, Effect of the anionic counterpart: Molybdate vs. tungstate in energy storage for pseudo-capacitor applications, Nanomaterials 11 (2021) 580, https://doi.org/10.3390/nano11030580.

[14] Z. Zhu, L. Zang, M. Chu, Y. He, D. Ren, P. Saha, Q. Cheng, Oxygen-vacancy and phosphorus-doping enriched NiMoO4 nanoarrays for high-energy supercapacitors, J. Energy Storage 54 (2022), 105314, https://doi.org/10.1016/j.est.2022.105314.

[15] B. Zhang, L. Wang, Z. Cao, S.M. Kozlov, F.P. García de Arquer, C.T. Dinh, J. Li, Z. Wang, X. Zheng, L. Zhang, High-valence metals improve oxygen evolution reaction performance by modulating 3d metal oxidation cycle energetics, Nat. Catal. 3 (2020) 985–992, https://doi.org/10.1038/s41929-020-00525-6.

[16] L. Sun, Y. Dang, A. Wu, C. Tian, D. Wang, H. Yan, Y. Gao, H. Fu, Synchronous regulation of morphology and electronic structure of FeNi-P nanosheet arrays by Zn implantation for robust overall water splitting, Nano Res (2022) 1–10, https://doi.org/10.1007/s12274-022-5245-y.

[17] Y. Li, H. Guo, J. Zhao, Y. Zhang, L. Zhao, R. Song, Te-doped NiFe2O4 stabilized by amorphous carbon layers derived from one-step topological transitions of NiFe LDHs with significantly enhanced oxygen evolution reaction, Chem. Eng. J. 464 (2023), 142604, https://doi.org/10.1016/j.cej.2023.142604.

[18] Y. Song, M. Sun, S. Zhang, X. Zhang, P. Yi, J. Liu, B. Huang, M. Huang, L. Zhang, Alleviating the work function of vein-like CoXP by Cr doping for enhanced seawater electrolysis, Adv. Funct. Mater. (2023), 2214081, https://doi.org/10.1002/adfm.202214081.

[19] J. Qian, X. Wang, H. Jiang, S. Li, C. Li, S. Li, R. Ma, J. Wang, Interfaces, Surface engineering of Cr-doped cobalt molybdate toward high-performance hydrogen

[20] evolution, ACS Appl. Mater. Interfaces 14 (2022) 18607–18615, https://doi.org/10.1021/acsami.2c03380.

[20] M.H. Wang, Z.X. Lou, X. Wu, Y. Liu, J.Y. Zhao, K.Z. Sun, W.X. Li, J. Chen, H. Y. Yuan, M. Zhu, Operando high-valence Cr-modified NiFe hydroxides for water oxidation, Small 18 (2022), 2200303, https://doi.org/10.1002/smll.202200303.

[21] Z. Wang, W. Liu, Y. Hu, M. Guan, L. Xu, H. Li, J. Bao, H. Li, Cr-doped CoFe layered double hydroxides: Highly efficient and robust bifunctional electrocatalyst for the oxidation of water and urea, Appl. Catal. B 272 (2020), 118959, https://doi.org/10.1016/j.apcatb.2020.118959.

[22] X. Li, X. Du, X. Zhang, Electronic modulation of Co2P nanoneedle arrays by the doping of transition metal Cr atoms for a urea oxidation reaction, Dalton Trans. 51 (2022) 13255–13262, https://doi.org/10.1039/D2DT02224A.

[23] X. Hu, G. Luo, X. Guo, Q. Zhao, R. Wang, G. Huang, B. Jiang, C. Xu, F. Pan, Origin of the electrocatalytic oxygen evolution activity of nickel phosphides: in-situ electrochemical oxidation and Cr doping to achieve high performance, Sci. Bull. 66 (2021) 708–719, https://doi.org/10.1016/j.scib.2020.11.009.

[24] L. Xia, J. Wang, L. Bo, W. Shi, Y. Zhang, Y. Shen, X. Ji, X. Guan, Y. Wang, J. Tong, Electronic structure modulation coupling with interface effect for great improving water electrolysis by multiple dimensional S doped MnCo2O4 nanorods/N doped C nanosheets hybrids, Chem. Eng. J. (2023), 143464, https://doi.org/10.1016/j.cej.2023.143464.

[25] S. Ding, J.A. Barr, Z. Lyu, F. Zhang, M. Wang, P. Tieu, X. Li, M.H. Engelhard, Z. Feng, S.P. Beckman, Effect of phosphorus modulation in iron single-atom catalysts for peroxidase mimicking, Adv. Mater. (2023), 2209633, https://doi.org/10.1002/adma.202209633.

[26] D.R. Paudel, U.N. Pan, T.I. Singh, C.C. Gudal, N.H. Kim, J.H. Lee, Fe and P doped 1T-phase enriched WS2 3D-dendritic nanostructures for efficient overall water splitting, Appl. Catal. B 286 (2021), 119897, https://doi.org/10.1016/j.apcatb.2021.119897.

[27] Y. Zhang, H. Guo, M. Song, L. Sun, R. Song, Modulation of the morphology and electronic structure of Ni3S2 nano-forests via P and Mo co-doping in polyoxometalates to promote the urea oxidation reaction, J. Mater. Chem. A 11 (2023) 3584–3593, https://doi.org/10.1039/D2TA08645J.

[28] C. Li, H. Jang, S. Liu, M.G. Kim, L. Hou, X. Liu, J. Cho, P and Mo dual doped Ru ultrasmall nanoclusters embedded in P-doped porous carbon toward efficient hydrogen evolution reaction, Adv. Energy Mater. 12 (2022), 2200029, https://doi.org/10.1002/aenm.202200029.

[29] T. Tang, W. Jiang, S. Niu, N. Liu, H. Luo, Y. Chen, S. Jin, F. Gao, L. Wan, J. Hu, Electronic and morphological dual modulation of cobalt carbonate hydroxides by Mn doping toward highly efficient and stable bifunctional electrocatalysts for overall water splitting, J. Am. Chem. Soc. 139 (2017) 8320–8328, https://doi.org/10.1021/jacs.7b03507.

[30] F. Herold, T. Imhof, P. Roumeliotis, P. Schühle, M. Ledendecker, M. Rønning, Controlled doping of carbon catalyst supports by atomic replacement via gasification-assisted heteroatom doping, Carbon 207 (2023) 207–218, https://doi.org/10.1016/j.carbon.2023.03.023.

[31] L. Guo, J. Chi, J. Zhu, T. Cui, J. Lai, L. Wang, Dual-doping NiMoO4 with multi-channel structure enable urea-assisted energy-saving H2 production at large current density in alkaline seawater, Appl. Catal. B 320 (2023), 121977, https://doi.org/10.1016/j.apcatb.2022.121977.

[32] Z. Liu, K. Wang, X. Tong, F. Kong, Y. Cao, Fuels, Deep reconstruction of Fe-NiMoO4·nH2O@NiOOH as efficient oxygen evolution electrocatalysts, Energy Fuels 37 (2023) 3023–3030, https://doi.org/10.1021/acs.energyfuels.2c03732.

[33] K. Eda, Y. Kato, Y. Ohshiro, T. Sugitani, M.S. Whittingham, Synthesis, crystal structure, and structural conversion of Ni molybdate hydrate NiMoO4·nH2O, J. Solid State Chem. 183 (2010) 1334–1339, https://doi.org/10.1016/j.jssc.2010.04.009.

[34] Y. Zhang, R. Yao, Y. Wu, Q. Zhao, J. Li, G. Liu, In situ rapid and deep self-reconstruction of Fe-doped hydrate NiMoO4 for stable water oxidation at high current densities, Chem. Eng. J. 461 (2023), 142081, https://doi.org/10.1016/j.cej.2023.142081.

[35] J. Zhu, J. Qian, X. Peng, B. Xia, D. Gao, Etching-induced surface reconstruction of NiMoO4 for oxygen evolution reaction, Nanomicro Lett. 15 (2023), 30, https://doi.org/10.1007/s40820-022-01011-3.

[36] Y. Zhu, C. Liu, S. Cui, Z. Lu, J. Ye, Y. Wen, W. Shi, X. Huang, L. Xue, J. Bian, Multistep dissolution of lamellar crystals generates superthin amorphous Ni(OH)2 catalyst for UOR, Adv. Mater. (2023), 2301549, https://doi.org/10.1002/adma.202301549.

[37] Z. Yin, Y. Huang, L. Jiang, C. Meng, Y. Wu, H. Liu, J. Wang, Revealing the in situ evolution of tetrahedral NiMoO4 micropillar array for energy-efficient alkaline hydrogen production assisted by urea electrolysis, Small Methods (2023), 2300028, https://doi.org/10.1002/sstr.202300028.

[38] G. Li, X. Qiao, Y. Miao, T. Wang, F. Deng, Synergistic effect of N-NiMoO4/Ni heterogeneous interface with oxygen vacancies in N-NiMoO4/Ni/CNTs for superior overall water splitting, Small (2023), 2207196, https://doi.org/10.1002/smll.202207196.

[39] L. Yue, C. Ma, S. Yan, Z. Wu, W. Zhao, Q. Liu, Y. Luo, B. Zhong, F. Zhang, Y. Liu, Improving the intrinsic electronic conductivity of NiMoO4 anodes by phosphorous doping for high lithium storage, Nano Res. 15 (2022) 186–194, https://doi.org/10.1007/s12274-021-3455-3.

[40] Y. Song, M. Sun, S. Zhang, X. Zhang, P. Yi, J. Liu, B. Huang, M. Huang, L. Zhang, Alleviating the Work Function of Vein-Like CoXP by Cr Doping for Enhanced Seawater Electrolysis, 33 (2023) 2214081, ⟨https://doi.org/10.1002/adfm.202214081⟩.

[41] Z. Xiao, M. Yang, J. Wang, Z. Xu, S. Zhang, A. Tang, R. Gao, H. Yang, FeNiP/MoOx integrated electrode grown on monocrystalline NiMoO4 nanorods with multi-

interface for accelerating alkaline hydrogen evolution reaction, Appl. Catal. B 303 (2022), 120913, https://doi.org/10.1016/j.apcatb.2021.120913.

[42] P. Zhou, G. Hai, G. Zhao, R. Li, X. Huang, Y. Lu, G. Wang, CeO$_2$ as an" electron pump" to boost the performance of Co$_4$N in electrocatalytic hydrogen evolution, oxygen evolution and biomass oxidation valorization, Appl. Catal. B (2023), 122364, https://doi.org/10.1016/j.apcatb.2023.122364.

[43] Q. Xu, Y. Liu, H. Jiang, Y. Hu, H. Liu, C. Li, Unsaturated sulfur edge engineering of strongly coupled MoS$_2$ nanosheet-carbon macroporous hybrid catalyst for enhanced hydrogen generation, Adv. Energy Mater. 9 (2019), 1802553, https://doi.org/10.1002/aenm.201802553.

[44] M. Chen, N. Kitiphatpiboon, C. Feng, Q. Zhao, A. Abudula, Y. Ma, K. Yan, G. Guan, Tuning octahedron sites in MnFe$_2$O$_4$ spinel by boron doping for highly efficient seawater splitting, Appl. Catal. B 330 (2023), 122577, https://doi.org/10.1016/j.apcatb.2023.122577.

[45] L. Ma, Z. Wei, C. Zhao, X. Meng, H. Zhang, M. Song, Y. Wang, B. Li, X. Huang, C. Xu, Hierarchical superhydrophilic/superaerophobic 3D porous trimetallic (Fe, Co, Ni) spinel/carbon/nickel foam for boosting oxygen evolution reaction, Appl. Catal. B 332 (2023), 122717, https://doi.org/10.1016/j.apcatb.2023.122717.

[46] S. Zhang, Y. Wang, X. Wei, L. Chu, W. Tian, H. Wang, M. Huang, Dual interface-reinforced built-in electric field for chlorine-free seawater oxidation, Appl. Catal. B 336 (2023), 122926, https://doi.org/10.1016/j.apcatb.2023.122926.

[47] P. Zhai, C. Wang, Y. Zhao, Y. Zhang, J. Gao, L. Sun, J. Hou, Regulating electronic states of nitride/hydroxide to accelerate kinetics for oxygen evolution at large current density, Nat. Commun. 14 (2023), 1873, https://doi.org/10.1038/s41467-023-37091-x.

[48] D.M. Morales, M.A. Kazakova, S. Dieckhöfer, A.G. Selyutin, G.V. Golubtsov, W. Schuhmann, J. Masa, Trimetallic Mn-Fe-Ni oxide nanoparticles supported on multi-walled carbon nanotubes as high-performance bifunctional ORR/OER electrocatalyst in alkaline media, Adv. Funct. Mater. 30 (2020), 1905992, https://doi.org/10.1002/adfm.201905992.

[49] K. Wang, S. He, B. Li, H. Du, T. Wang, Z. Du, L. Xie, W. Ai, Relaying alkaline hydrogen evolution over locally amorphous Ni/Co-based phosphides constructed by diffusion-limited phase-transition, Appl. Catal. B Environ. 339 (2023), 123136, https://doi.org/10.1016/j.apcatb.2023.123136.

[50] Y. Gan, Y. Ye, X. Dai, X. Yin, Y. Cao, R. Cai, X. Zhang, Self-sacrificial reconstruction of MoO$_4^{2-}$ intercalated NiFe LDH/Co$_2$P heterostructures enabling interfacial synergies and oxygen vacancies for triggering oxygen evolution reaction, J. Colloid Interface Sci. 629 (2023) 896–907, https://doi.org/10.1016/j.jcis.2022.09.125.

[51] M.R. Kandel, U.N. Pan, P.P. Dhakal, R.B. Ghising, T.T. Nguyen, J. Zhao, N.H. Kim, J.H. Lee, Unique heterointerface engineering of Ni$_2$P-MnP nanosheets coupled Co$_2$P nanoflowers as hierarchical dual-functional electrocatalyst for highly proficient overall water-splitting, Appl. Catal. B 331 (2023), 122680, https://doi.org/10.1016/j.apcatb.2023.122680.

[52] L. Qiao, A. Zhu, D. Liu, J. Feng, Y. Chen, M. Chen, P. Zhou, L. Yin, R. Wu, K.W. Ng, Crystalline phosphides/amorphous oxides composite for energy-saving hydrogen production assisted by efficient urea oxidation reaction, Chem. Eng. J. 454 (2023), 140380, https://doi.org/10.1016/j.cej.2022.140380.

[53] P. Zhou, G. Hai, G. Zhao, R. Li, X. Huang, Y. Lu, G. Wang, CeO$_2$ as an "electron pump" to boost the performance of Co$_4$N in electrocatalytic hydrogen evolution, oxygen evolution and biomass oxidation valorization, Appl. Catal. B 325 (2023), 122364, https://doi.org/10.1016/j.apcatb.2023.122364.

[54] Y. Zhou, Y. Wang, D. Kong, Q. Zhao, L. Zhao, J. Zhang, X. Chen, Y. Li, Y. Xu, C. Meng, Revealing the reactant mediation role of low-valence Mo for accelerated urea-assisted water splitting, Adv. Funct. Mater. 33 (2023), 2210656, https://doi.org/10.1002/adfm.202210656.